Volcanic eruption tremor from particle impacts and turbulence using conduit flow models

Katherine R. Coppess [1], **Fredric Y. K. Lam** [2], **Eric M. Dunham** [*2,3]

[1]Department of Physics, Stanford University, CA, USA, [2]Institute for Computational and Mathematical Engineering, Stanford University, Stanford, CA, USA, [3]Department of Geophysics, Stanford University, CA, USA

Author contributions: *Conceptualization*: Eric M. Dunham. *Methodology*: Katherine R. Coppess, Fredric Y.K. Lam, Eric M. Dunham. *Software*: Fredric Y.K. Lam. *Validation*: Katherine R. Coppess. *Formal Analysis*: Katherine R. Coppess, Eric M. Dunham. *Investigation*: Katherine R. Coppess, Fredric Y.K. Lam, Eric M. Dunham. *Resources*: Eric M. Dunham. *Writing - Original draft*: Katherine R. Coppess. *Writing - Review & Editing*: Eric M. Dunham. *Visualization*: Katherine R. Coppess. *Supervision*: Eric M. Dunham. *Project administration*: Eric M. Dunham. *Funding acquisition*: Katherine R. Coppess, Eric M. Dunham.

Abstract The intensity of explosive volcanic eruptions is correlated with the amplitude of eruption tremor, a ubiquitously observed seismic signal during eruptions. Here we expand upon a recently introduced theoretical model that attributes eruption tremor to particle impacts and dynamic pressure changes in the turbulent flow above fragmentation (Gestrich et al., 2020). We replace their point source model with Rayleigh wave Green's functions with full Green's functions and account for depth variation of input fields using conduit flow models. The latter self-consistently capture covariation of input fields like particle velocity, particle volume fraction, and density. Body wave contributions become significant above 2-3 Hz, bringing the power spectral density (PSD) closer to observations. Conditions at the vent are not representative of flow throughout the tremor source region and using these values overestimates tremor amplitude. Particle size and its depth distribution alter the PSD and where dominant source contributions arise within the conduit. Solutions with decreasing mass eruption rate, representing a waning eruption, reveal a shift in the dominant tremor contribution from turbulence to particle impacts. Our work demonstrates the ability to integrate conduit flow modeling with volcano seismology studies of eruption tremor, providing an opportunity to link observations to eruptive processes.

1 Introduction

Volcanic eruption tremor is a universally observed seismic signal from explosive eruptions within the 0.5-10 Hz frequency band. It is characterized by its coincidence with explosive eruptions and its incoherence, distinguishing itself from harmonic and pre-eruptive tremor (Chouet and Matoza, 2013; Matoza and Roman, 2022). Hereafter, we use the term "tremor" to refer to eruption tremor, which is the focus of our study. McNutt and Nishimura (2008) compiled

*Corresponding author: edunham@stanford.edu

examples of tremor from several different eruptions and found that the temporal evolution of the tremor amplitude during the course of an eruption followed similar trends: an initial stage of exponential increase, followed by a period of maintaining maximum amplitude, ending with an exponential decrease in amplitude. There have also been a number of empirical relationships observed between tremor amplitude and eruption parameters, such as vent cross-sectional area, volcanic explosivity index (VEI), and ash plume height (McNutt and Nishimura, 2008; McNutt, 1994). These commonalities across different events could indicate common physical processes occurring during sustained eruptions. Leveraging the apparent connection between eruption tremor source and other eruption parameters (e.g., plume height) has motivated the use of tremor to make real-time assessments of eruption size and intensity (Haney et al., 2018; McNutt, 1994; McNutt and Nishimura, 2008; Ichihara, 2016; Caplan-Auerbach et al., 2010; Prejean and Brodsky, 2011). This is important for evaluating aviation hazard from eruption plumes.

However, there are several examples of tremor deviating from the average behavior. During the 2016 eruption of Pavlof Volcano, Alaska, tremor amplitude and plume height evolved proportionally in the early stages of the eruption; but during the final stage, tremor amplitude decreased while the plume height remained high, deviating from what the empirical relation between the two would suggest (Fee et al., 2017). Clearly, there is a need to gain a better understanding of the tremor source to improve the utility of tremor in hazard assessments. Tremor is also often observed in infrasound (acoustic) data, as studied for the 2016 Pavlof eruption. Similarity between acoustic and seismic tremor amplitudes throughout the event suggests they share the same source, which would require coupling to both the atmosphere and the earth (Gestrich et al., 2020).

Gestrich et al. (2020) propose a tremor source mechanism arising from particle impacts and turbulence within the conduit above the fragmentation depth. The authors aim to reproduce the spectral content of seismic tremor generated during sustained explosive eruptions by adapting power spectral density (PSD) models of riverbed seismicity. A hysteresis between tremor amplitude and water level – similar to the one observed at Pavlof between tremor amplitude and plume height – was observed in fluvial systems, which Tsai et al. (2012) found could be explained by dynamic pressure changes arising from turbulent flow and impacts along the river-bottom of particles eroded from the riverbed. As the flow increases, erosion of the bed leads to large particles being carried along in the turbulent flow and colliding with the interface; eventually, the high particle load is cleared, leading to reduction in impacts even though the water level remains high. Eruptive flow in volcanic conduits above fragmentation exhibits similar characteristics: it is a particle-laden fluid comprised of magma clasts and eroded lithics carried by turbulent gas, which flows along a rough surface (the conduit walls) in response to a pressure gradient (the driving overpressure gradient countering gravity). Some notable differences between the two systems include the suspension fluid and geometry/orientation with respect to gravity.

Adapting this fluvial model, Gestrich et al. (2020) present one of the few theoretical studies of the eruption tremor source. The authors develop a point-source PSD model taking into account the different geometry and flow parameters for the eruption, and then convolving forces arising from particle-impacts and turbulence with Rayleigh-wave Green's functions to obtain the seismic response. As a simplifying approximation, they assume spatially uniform values for eruption parameters such as the particle velocity and particle volume fraction, whereas these may vary considerably in the conduit above fragmentation. They performed a sensitivity analysis of the input parameters,

finding that the representative grain size of the particles and the seismic wave propagation properties had the largest impact on the PSD. However, when comparing the model with observations at Pavlof, extreme parameter values (in particular, large grain sizes ≈0.5 m) were required to match the observed seismic PSD. The proposed explanation for the observed hysteresis is a reduction in grain size as the eruption progressed. The extreme parameter value requirements indicates this model may not be generally applicable, or that certain simplifying approximations in the model formulation need to be relaxed.

We expand on this work by generalizing components of the particle impacts and turbulence (referred to in this work as PIT) tremor model to utilize more realistic descriptions of the conditions in which tremor occurs. First, we use full Green's functions to describe seismic wave propagation, instead of Rayleigh-wave only. We find that accounting for body wave contributions in addition to surface waves increases the PSD amplitude by up to 70 dB in the >2.5 Hz band. We also adapt the PIT model to allow for depth variations of the tremor source properties. This allows us to use a conduit flow model to provide the depth-dependent density, velocity, and particle volume fraction throughout the conduit. We apply the modified particle impacts and turbulence (referred to as mPIT) model to solutions from a steady-state conduit flow model, but note that the formulation could be equally well applied to an unsteady conduit flow model to capture the time evolution of tremor over the course of an eruption. We leave this for future work. Instead, we explore the influence of spatially variable velocity, particle volume fraction, and grain size throughout the conduit on predicted tremor. In addition, we use a sequence of steady state models with different mass eruption rates (obtained by varying chamber pressure) to explore the evolution of tremor over the course of a waning eruption.

2 Summary of particle impacts and turbulence tremor source models

Here we present an overview of the model components; for more specifics, we refer the reader to Gestrich et al. (2020). Focus is restricted to the region above fragmentation, where flow is turbulent. This is also consistent with the hypothesis that the similarity in acoustic and seismic signal indicates source coupling to both the earth and the atmosphere. The authors also focus on vertical component velocity seismograms. The authors build up one-sided velocity PSD models for particle impacts and turbulence separately, assuming that particle impacts and dynamic pressure changes from turbulence are random and uncorrelated. The total PSD model is the superposition of the two. There are three components needed to calculate the PSD: a description of seismic wave propagation (i.e., Green's functions), how much momentum gets imparted to the surrounding earth, and how frequently does momentum transfer occur. Below we summarize the decisions and assumptions made by Gestrich et al. (2020) to define each of these components for the two source models.

For sufficiently shallow sources (e.g., depths much less than the wavelength of the target frequency $\lambda = v/f =$ 2000 m/s / 1 Hz = 2 km), the authors approximate the Green's function using surface-to-surface Green's functions, as well as treating the forces on the conduit walls as point sources acting in different directions. In addition, by considering only the vertical component of the seismograms, the authors make the simplifying assumption that Rayleigh waves will likely dominate the signal. The vertical component of the Green's function used for a force acting

in direction i takes the following form:

$$G_{zi} \approx \frac{k}{8\rho_s v_c v_u} N_i \sqrt{\frac{2}{\pi k r}} e^{-\pi f r/(v_u Q)}, \tag{1}$$

where $k = 2\pi f/v_c$ is wave number, ρ_s is solid density, Q is the Rayleigh-wave quality factor, r is source-receiver distance, v_c and v_u are the Rayleigh-wave phase and group velocity, and $N = (0.8, 0, 0.6)$ for radial, tangential, and vertical forces captures the horizontal/vertical ratio of Rayleigh wave eigenfunctions associated with the density and velocity profile of a generic rock site (Boore and Joyner, 1997; Gimbert et al., 2014). The Rayleigh wave phase and group velocities were calculated using a generic volcano velocity model from Lesage et al. (2018).

The volcanic conduit is assumed to be a vertically oriented cylinder with rough walls modeled with roughness half-spheres of varying diameters (see Figure 2 in Gestrich et al. (2020)). Particles are assumed to preferentially interact with roughness spheres of the same size, leading to an impact rate defined as

$$R_{\text{impact}} = \frac{\delta u}{D^3} \phi_p p(D), \;\; \delta u = 0.1 u_0, \tag{2}$$

where δu is the magnitude of velocity fluctuations, ϕ_p is the particle volume fraction, u_0 is the mean flow velocity, D is particle grain size, and $p(D)$ is the grain size distribution. This means that larger particles impact less often because fewer large roughness spheres can fit between the fragmentation depth and the vent. The impact force from the particle collisions along the walls is treated as an impulse force. It is assumed that only the component of the force normal to a roughness sphere (not necessarily normal to the conduit) imparts momentum to the earth. The particle velocity at impact is composed of two contributions: the mean flow velocity and fluctuations about the mean flow due to turbulence. The mean flow velocity is assumed to be only in the vertical direction and varying only radially (i.e., independent of depth). The radial velocity profile is chosen to follow a logarithmic profile for turbulent flows in rough pipes. The flow velocity at the maximum roughness height sets the mean flow velocity. The authors assume that the turbulence in the flow is isotropic, which means that fluctuations around the mean flow velocity are equal in all directions. Therefore, they define random directions and unit impulses associated with these fluctuations and integrate over all impact angles, assuming that roughness is statistically symmetric around the conduit:

$$F_{x,y} \approx 0.36(1 + e_b) m u_0, \;\; F_z \approx 0.29(1 + e_b) m u_0, \tag{3}$$

where e_b is the coefficient of restitution and m is the particle density (assumed to be same as average rock density). These can then be combined to calculate the particle impacts PSD, after performing a surface integral over the conduit walls above fragmentation:

$$PSD_{\text{impact}} = \int_D 2\pi \hat{R} d_f R_{\text{impact}} \left(2\pi f \sum_j F_j G_{zj} \right)^2 dD, \tag{4}$$

where $\hat{R}$ is the conduit radius and d_f is fragmentation depth. The full expression for the particle impacts PSD for the

PIT model is as follows:

$$PSD_{\text{impact}} \approx 5.8\,\overline{u}_0^3 f^3 (1+e_b)^2 \phi_p D_r^3 \frac{\hat{R} d_f}{r v_c^3 v_u^2} e^{-2\pi f r/(v_u Q)}, \tag{5}$$

where $D_r = (\int_D D^3 p(D) dD)^{1/3}$ is the representative grain size.

The random eddies in the turbulent flow lead to velocity fluctuations that cause dynamic pressure changes along the conduit wall, exciting elastic waves. Therefore for the turbulence model, the authors define a force spectrum $\tilde{F}$ – instead of defining impact rate and force separately – using the velocity spectrum associated with turbulent flow. Assuming that forces in different directions are independent, the turbulence PSD can be formulated as follows:

$$PSD_{\text{turbulence}} = 8\pi^3 \hat{R} d_f f^2 \sum_j \tilde{F} G_{zj}^2, \tag{6}$$

where $\tilde{F}$ is the force spectrum on the walls per unit length of the conduit (units of $\text{N}^2\text{m}^{-1}\text{Hz}^{-1}$). To calculate the velocity spectrum, the authors follow Gimbert et al. (2014) and assume that the turbulence at the point of maximum roughness of the conduit walls is in the inertial subrange (i.e., the boundary layer is very thin and approximated by wall roughness height D_b), where the Kolmogorov velocity spectrum can be used:

$$E_K = K \epsilon^{2/3} k_t^{-5/3}, \tag{7}$$

where $K = 0.5$ is the Kolmogorov universal constant, $k_t = 2\pi f / \overline{u}_z(r)|_{r=\hat{R}-D_b/4}$ is the wave number of velocity fluctuations, and ϵ is the dissipation rate. This holds for very large Reynolds numbers, like those observed in explosive volcanic jets. In this subrange, energy dissipation and production associated with the break-up of turbulent eddies are assumed to be equal. Therefore, the dissipation rate is defined using the energy production rate from breaking up of larger eddies:

$$\epsilon(r)|_{r=\hat{R}-D_b/4} = \frac{1}{\kappa} \frac{u_*^3}{D_b/4}, \tag{8}$$

where $\kappa = 0.4$ is the Von Karman constant and $u_* = 0.06\overline{u}_0$ is the shear velocity. The authors then use Taylor's frozen-turbulence hypothesis to define the velocity spectrum in frequency domain:

$$\tilde{E}_K = \frac{2\pi}{\overline{u}_z(r)|_{r=\hat{R}-D_b/4}} E_K. \tag{9}$$

The force spectrum is calculated by finding the drag force on a roughness half sphere from the velocity fluctuations described by the velocity spectrum:

$$\tilde{F}_p \approx (C \rho_g \overline{u}_z(r)|_{r=\hat{R}-D_b/4} A)^2 \tilde{E}_K \chi_{\text{fl}}^2, \tag{10}$$

where $C = 0.5$ is the drag coefficient, ρ_g is the gas density, $A = \pi D_b^2/4$ is the area the force is applied over, and $\chi_{\text{fl}} = 1$ is the fluid-dynamic admittance. Note that they assume a fixed roughness height and that force time series for different roughness patches are uncorrelated. Thus, superposition of the force contributions from all roughnesses

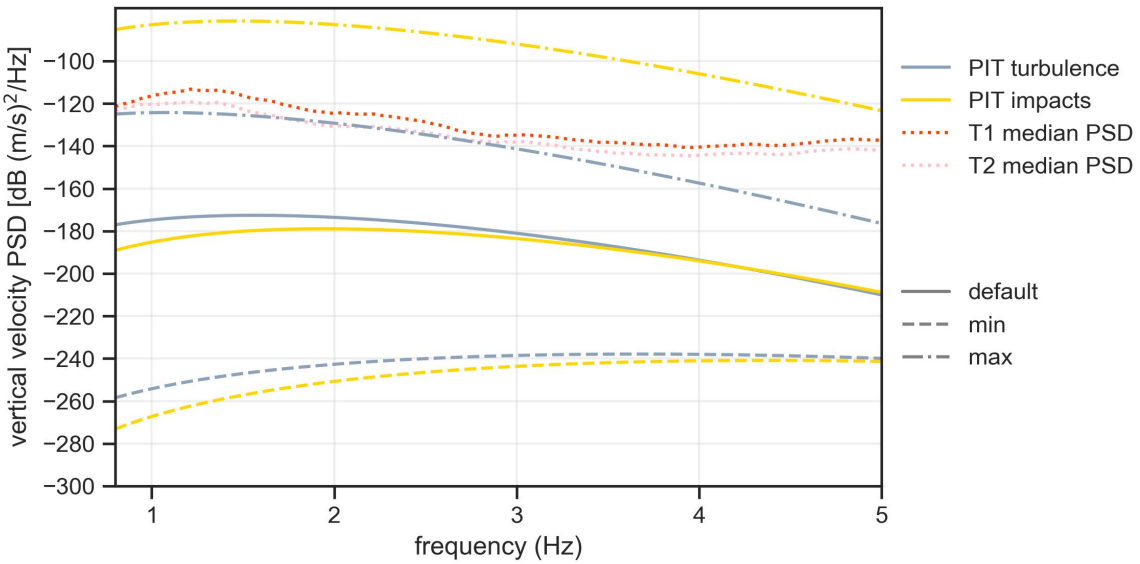

Figure 1 Recreation of Figure 10 from Gestrich et al. (2020), but using the corrected expressions and the stated parameter ranges. Observed seismic PSDs from 2016 Pavlof eruption are plotted with dotted lines: T1 (red) is the period of sustained maximum seismic amplitude and T2 (pink) is the period of seismic amplitude decrease.

is given by

$$\tilde{F} = N_p \tilde{F}_p = \frac{\tilde{F}_p}{D_b^2}, \tag{11}$$

where N_p is the number of roughness half spheres per unit area of the conduit walls. Putting this all together, the final expression for the turbulence PSD for the PIT model is

$$PSD_{\text{turbulence}} \approx 0.0011 \bar{u}_0^{14/3} f^{4/3} D_b^{4/3} \frac{\rho_g^2}{\rho_s^2} \frac{\hat{R} d_f}{r v_c^3 v_u^2} e^{-2\pi f r/(v_u Q)}. \tag{12}$$

It is important to note that the final expressions stated in equations (28) and (29) of Gestrich et al. (2020) have incorrect values for the numerical prefactors, likely due to algebra errors. It also seems that the min-max parameter values used in Figure 10 in Gestrich et al. (2020) are inconsistent with the stated parameter ranges and figures demonstrating parameter sensitivity. Figure 1 is a recreation of this figure from Gestrich et al. (2020) using the corrected expressions and the stated parameter ranges. When looking at the default values used by Gestrich et al. (2020), this correction highlights the comparable contributions of particle impacts and turbulence to the seismic spectrum at higher frequencies (>2.5 Hz), with turbulence yielding a larger contribution at low frequencies. Both contributions experience the same level of attenuation at high frequencies but the impacts model has a stronger dependence on frequency, which counteracts the attenuation more strongly. Therefore, the impacts PSD model experiences a smaller reduction in power as frequency increases, leading to similar power compared with the turbulence PSD. Also plotted in Figure 1 are the observed seismic PSD data taken during two periods of the 2016 Pavlof eruption: the period during sustained maximal seismic amplitude (T1) and when seismic amplitude decreased while plume height remained high (T2). We refer readers to Figure 1 in Gestrich et al. (2020) for more context with acoustic and plume height data. We follow the same data processing scheme as Gestrich et al. (2020): data taken from Station PS1A (about 9.5 km from the vent) is band-pass filtered between 0.5 and 8 Hz and the PSD is smoothed using a sliding median window

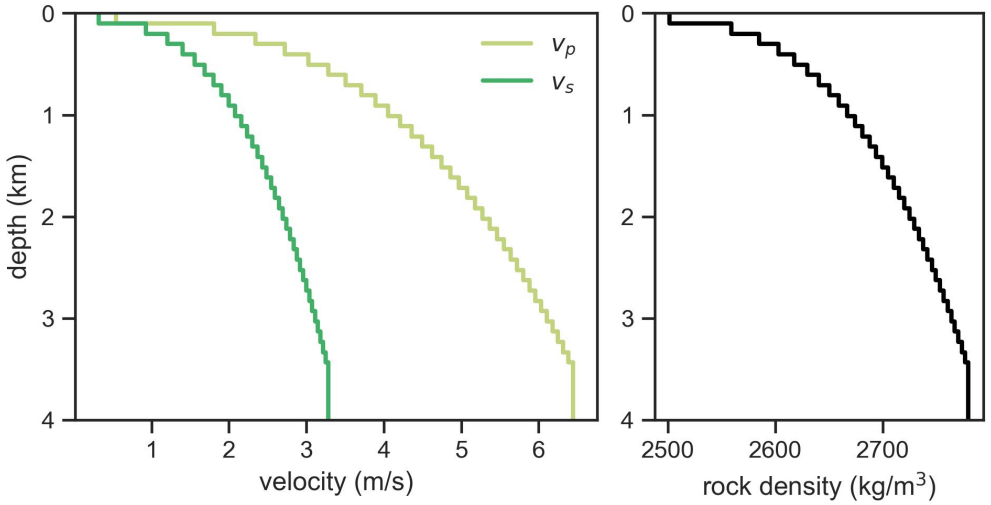

Figure 2 P-wave and S-wave velocity (v_p and v_s)and density profiles used to calculate full numerical Green's functions. Velocity profiles are from the generic volcano model in (13). Density is obtained using empirical correlations in (14).

of 0.33 Hz length. When comparing the model outputs to the observed PSDs, Gestrich et al. (2020) found that only the maximum particle impacts PSD of the PIT model could recreate the observed power. Given the corrections, it appears that inputs solidly within the considered range for impact PSDs and the maximum possible turbulence PSD may be able to reproduce the observed power. However, we find with the mPIT model (presented in the next section) that very extreme parameter values will still be required to reach observed power.

3 Model modifications

In this study, we modify the particle impacts and turbulence (PIT) tremor model developed by Gestrich et al. (2020) in two ways: 1) replacing the Rayleigh-wave-only Green's functions with full Green's functions, and 2) extending it to allow for depth variation of input fields. We then apply the modified PIT (mPIT) model to results from conduit flow simulations.

The full Green's functions are numerically calculated using the frequency-wavenumber method (Zhu and Rivera, 2002). Figure 2 shows the velocity and density profiles with depth used to capture the surrounding earth's material structure. For consistency with choices made in Gestrich et al. (2020), we use the generic volcano model from Lesage et al. (2018) for the velocity profile $v(z)$:

$$v(z) = v_0 \left[\left(\frac{z+a}{1\,\mathrm{m}} \right)^{\alpha} - \left(\frac{a}{1\,\mathrm{m}} \right)^{\alpha} + 1 \right], \tag{13}$$

where z is depth in meters and the fit parameters for P and S waves are: [$v_{p0} = 540$ m/s, $\alpha_p = 0.315$, $a_p = 10$ m] and [$v_{s0} = 320$ m/s, $\alpha_s = 0.3$, $a_s = 15$ m]. These parameters were empirically determined in Lesage et al. (2018) by fitting (13) up to 500 m depths of velocity structure data from different volcanoes. We extend this profile to 3.5 km, at which point the P- and S-wave velocities become unrealistically high; below that, the velocity structure is for a homogeneous half-space. For the rock density profile, we follow Gimbert et al. (2014) and use the empirical relationship between

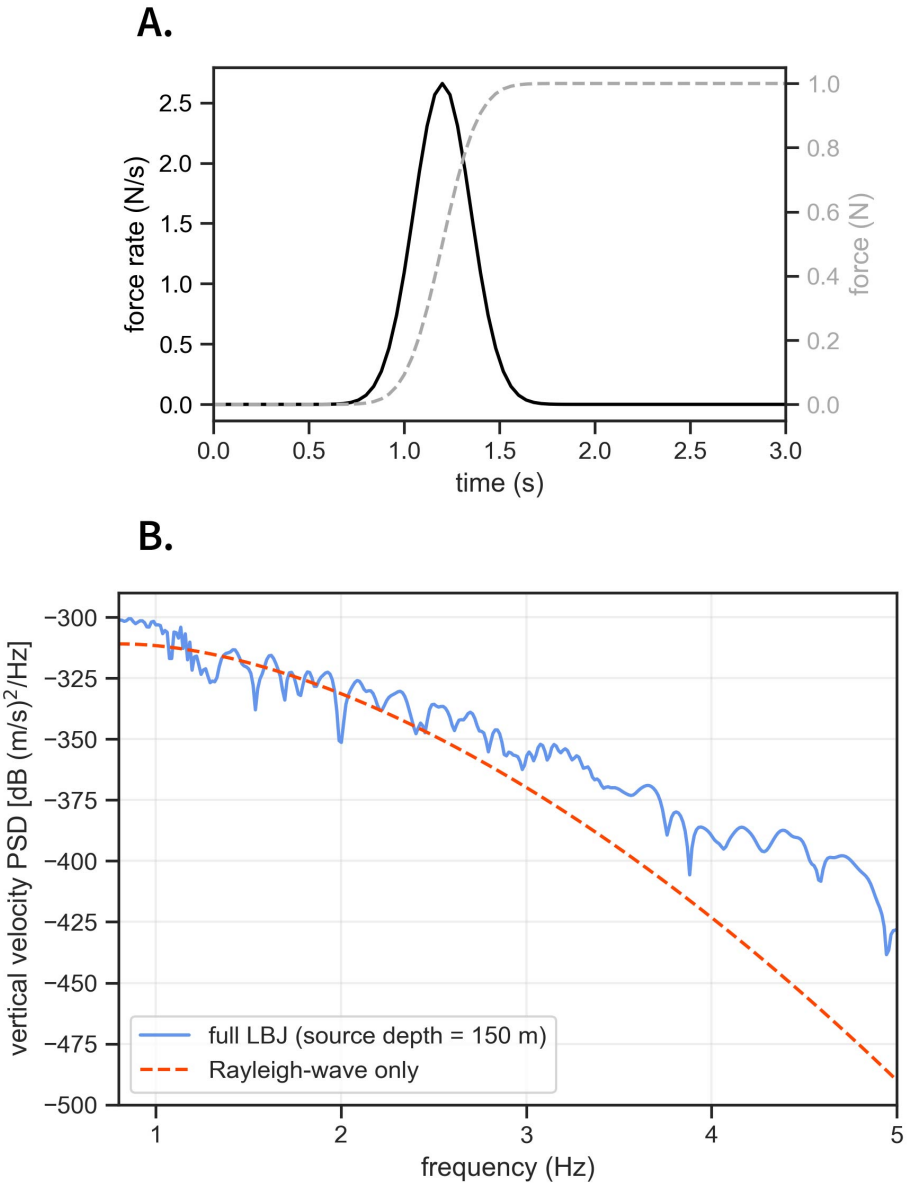

Figure 3 **A.** Force and force rate history convolved with Green's functions. **B.** Comparison of full LBJ Green's functions (source depth at 150 m) with Rayleigh-wave only Green's functions at a station located 10 km away, both convolved with the force rate history shown in **A**. Results are for the vertical component of velocity seismograms from a vertical force: $\dot{F}G_{zz}$.

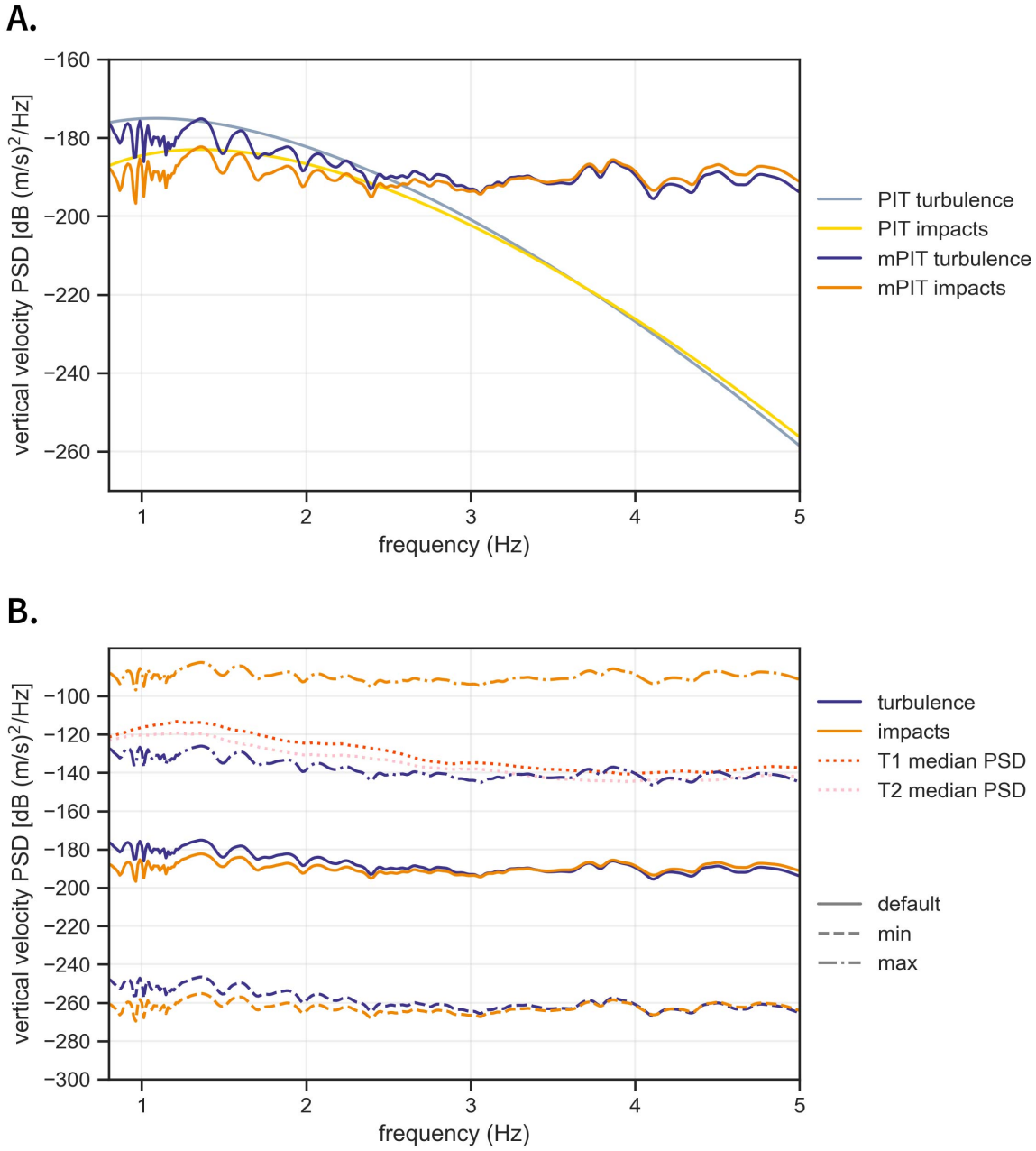

Figure 4 Recreation of Figure 10 from Gestrich et al. (2020) comparing the PIT and mPIT models. In this calculation, the input fields are assumed to be depth independent. **A.** Default values used in Gestrich et al. (2020). **B.** Min-max inputs as used in Figure 1 in mPIT model. Observed seismic PSDs from 2016 Pavlof eruption are plotted with dotted lines: T1 (red) is the period of sustained maximum seismic amplitude and T2 (pink) is the period of seismic amplitude decrease.

rock density and S-wave velocity developed by Boore and Joyner (1997):

$$\rho_s = 2500 + 93.75 \left[\frac{v_s}{1\,\text{km/s}} - 0.3 \right], \tag{14}$$

where density is in units of kg/m^3. To account for attenuation, Zhu and Rivera (2002) assume that the P-wave quality factor is twice the S-wave quality factor, which we set to 30. Figure 3 (b) shows a comparison between PSDs when convolving a Gaussian (i.e. approximated delta) force-rate history (Figure 3 (a)) with the Rayleigh wave Green's function (with quality factor of 30) and the full Lesage-Boore-Joyner (LBJ) Green's functions. At lower frequencies, the signal PSD is dominated by Rayleigh waves, consistent with the assumptions of Gestrich et al. (2020). However, at the higher end of the tremor frequency range (>2.5 Hz), considering only the Rayleigh waves underestimates the power. The difference reaches around 70 dB at 5 Hz, which corresponds to 7 orders of magnitude.

Extending the model to allow depth variation of input parameters is straightforward. We treat the conduit as a distribution of point sources, as described in Coppess et al. (2022). We apply the PIT model with full Green's functions to each point source, replacing the dependence on fragmentation depth d_f with grid spacing dz (which comes from the surface integral along the conduit walls). The source-receiver distance and orientation are already accounted for in the numerical Green's functions. Then all the PSD contributions are summed together to get the total PSD.

In addition to the use of different Green's functions in the PIT vs mPIT models, there is an additional difference arising from assuming a point-source (PIT) vs extended-source (mPIT). The extended source calculation involves different radiation patterns and different source-receiver distances for different depth source contributions. Given the shallow depths and the station distances considered here, this effect is not as pronounced as that from using different Green's functions. Figure 4 shows a comparison of the PIT and mPIT models, assuming the same spatially uniform default parameter values used in Figure 1 and in Gestrich et al. (2020) (this will not be the case for the remaining examples in this work). The frequency of maximum power (approximately 1.5 Hz) is consistent between the two models. However, the PSD shape is altered by using LBJ Green's functions, yielding a flatter spectrum across the 1-5 Hz frequency band. The discrepancy between the two sets of Green's function widens as frequency increases beyond 2.5 Hz and reaches around a 70 dB difference, consistent with what we observed in the simpler delta force-rate point source example (Figure 3). As shown in Figure 4, this flat spectrum is more consistent with the observed spectrum in the 2016 Pavlof eruption.

4 Applying tremor model to steady-state conduit flow

In this section, we apply the mPIT model to steady-state conduit flow solutions. We use an adiabatic quasi-1D multiphase steady-state conduit flow model that solves governing equations for mass, momentum, and energy balance. All phases (melt, water, and crystals) are assumed to be co-moving and share the same temperature and pressure at a given depth. Modeled processes include exsolution of volatiles from the melt and magma fragmentation. Fragmentation is modeled using a critical volume fraction criterion, where drag is reduced to zero when the exsolved gas volume fraction exceeds some threshold. Magma viscosity depends on dissolved volatile and crystal content, calculated using the empirical expressions in Hess and Dingwell (1996) (their equation 7) and Costa (2005) (their equation 2 in Comments). For specifics on the conduit flow model, we refer the reader to Appendix A in Coppess et al. (2024).

Table 1 Parameter values used in steady-state solution in Section 4.1. **Bold** indicates parameters that are changed in later sections.

Symbol	Description	Numerical value
g	gravitational acceleration	9.8 m/s^2
ϕ_0	critical gas volume fraction (with respect to total volume)	0.75
$t_{\rm ex}$	exsolution timescale	10 s
S_m	solubility constant	5×10^{-6} Pa$^{1/2}$
χ_0	water mass concentration at chamber	0.03
ϕ_c	bulk crystal volume fraction (with respect to magma volume)	0.4
R_G	specific gas constant	461 J/(kg K)
$T_{\rm ch}$	chamber temperature	1050 K
$p_{\rm ch}$	**chamber pressure**	90 MPa
K	magma bulk modulus	10^9 Pa
$\rho_{\rm mag,0}$	reference magma density	2600 kg/m^3
p_0	exsolution pressure	n_0^2/S_m^2
$C_{\rm v,ex}$	exsolved water heat capacity	1827 J/(kg K)
$C_{\rm v,mag}$	magma heat capacity	3000 J/(kg K)
R	conduit radius	20 m
L	conduit length	3 km

[Reviewers: Coppess et al. (2024) is under review. A pdf version has been provided along with this submission so that you can read more about the conduit flow model.] Only the relevant field values above the fragmentation depth are used for tremor model input. Since particles are not explicitly modeled, we define the particle volume fraction as the fraction of the mixture volume excluding exsolved gas. Table 1 provides model parameter values used to calculate solutions used in the following sections.

We perform a parameter study to learn how different characteristics of the steady-state solution and input field depth profiles influence the seismic PSD. In the final section, we use the steady-state model to represent time snapshots of a waning eruption with decreasing mass eruption rate (obtained by decreasing chamber pressure).

4.1 Comparison of PIT and mPIT results

The steady state solutions are calculated for a 3 km-long conduit, with fragmentation occurring around 2 km depth in the reference case. The total volatile content is 3 wt% and crystal volume fraction (volume of crystal phase / volume of magma, where magma refers to the mixture of melt and dissolved gas) is depth-invariant at a value of 0.4. Magma is injected through the bottom boundary at a pressure of 90 MPa (in the reference case). As the magma rises through the conduit, it depressurizes due to drag along the conduit walls and relief of the overlying weight. Depressurization of the magma leads to volatile exsolution (i.e., formation and growth of bubbles). Eventually, the mixture will become so bubbly that the liquid matrix containing the bubbles will no longer be stable or strong enough to sustain the bubbly mixture. At this point, the mixture undergoes fragmentation, whereby the mixture suddenly breaks apart and accelerates gas and magma fragments upward toward the vent. Figure 5 shows the mPIT input fields above fragmentation. The reduction in drag that accompanies fragmentation leaves unbalanced forces, accelerating the mixture upward. This is accompanied by depressurization and expansion of the gas (i.e., reduction of particle volume fraction). The mixture continues to accelerate as it approaches the vent. In the reference case simulation, the bottom pressure is sufficiently high that flow chokes at the vent (i.e., magma is erupted out at the mixture sound speed). Other simulations used later to illustrate changes in eruption tremor as mass eruption rate decreases feature subsonic outflow, and for those simulations we set pressure at the vent to atmospheric.

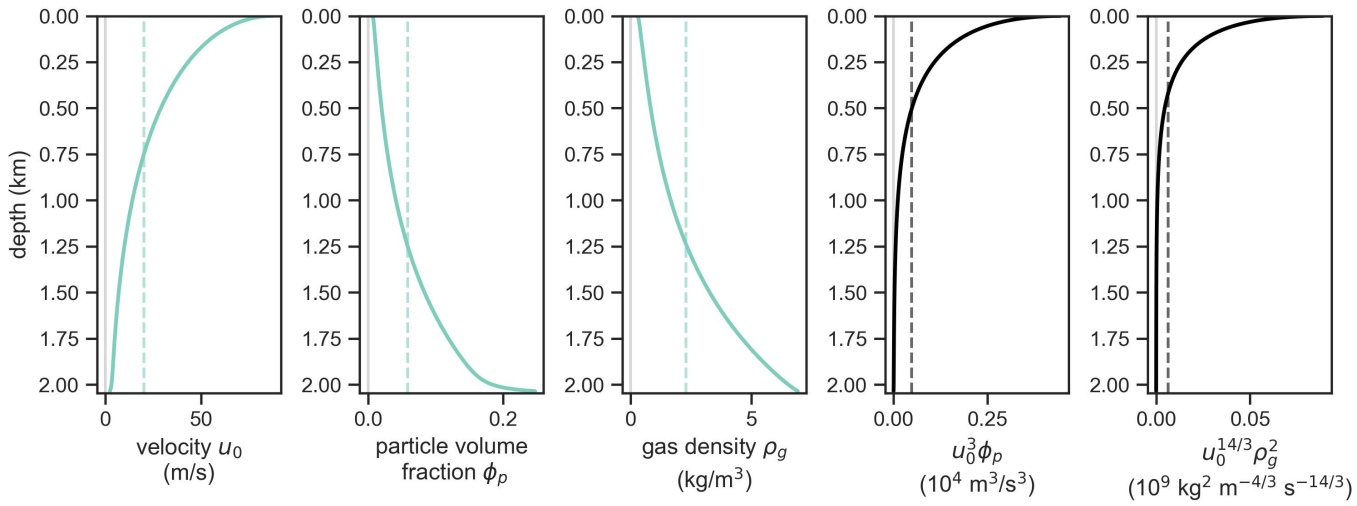

Figure 5 Fields above fragmentation depth from steady-state conduit flow model. Parameter values are listed in Table 1. In the left three panels, vertical dashed lines mark the depth-averaged values of the field over the region plotted: $\langle u_0 \rangle = 20.2$ m/s, $\langle \phi_p \rangle = 0.059$, $\langle \rho_g \rangle = 2.29$ kg/m^3. The dashed lines in the right two panels correspond to $\langle u_0 \rangle^3 \langle \phi_p \rangle$ and $\langle u_0 \rangle^{14/3} \langle \rho_g \rangle^2$, respectively (i.e. the value calculated from inputting the averaged field values into the expression indicated on the x-axes).

The final two panels in Figure 5 show how the input fields taken from the steady-state solution translate into the depth profiles of parameter combinations appearing in the integrand of the particle impacts ($u_0^3 \phi_p$) and turbulence ($u_0^{14/3} \rho_g^2$) force spectra. The velocity field has the most significant impact on the depth profiles, as both models depend strongly on the mean flow speed. Both models' profiles increase with decreasing depth, with the largest contribution at the vent, despite the much reduced particle volume fraction and gas density. Even though the fragmentation depth is around 2 km, the largest contributions are contained within the top 500 m of the conduit. The associated tremor PSDs using mPIT are shown in Figure 6 (solid lines). For the remaining inputs not modelled in our conduit flow model, we assume a constant depth profile with the same default values used in Gestrich et al. (2020): representative grain size $D_r = 1.4 \times 10^{-3}$ m and roughness size $D_b = 0.5$ m.

We investigate the role of depth variation of the input fields by assuming a constant profile of the depth-averaged field values (i.e., averaging over the region above fragmentation), which are shown with dashed lines in Figure 5. These results are represented by the dashed lines in Figure 6. Comparing the two mPIT results, using the depth-averaged values underestimates the spectral power by a few dB, with greater impact at lower frequencies. The spectral shape seems to be reasonably captured by the averaged inputs, indicating that the modeling of wave propagation has the larger influence on the calculated PSD than accounting for the depth variation of the input fields. This provides further justification for neglecting depth variation above fragmentation, as was done in Gestrich et al. (2020). However, it is still important to take depth variation into account when choosing what value to use to represent the input field. Consider the velocity profile, for instance (Figure 5). Flow velocity varies significantly over the whole region above fragmentation; the depth-averaged flow velocity is significantly less than the peak velocity reached at the vent. Even though high exit velocities can be achieved, that does not mean that they are representative of flow throughout the upper conduit. Thus, conditions at the vent are likely not representative of the whole region above fragmentation. This places even more stringent restrictions on the range of input values that would be reasonable to consider, which will limit the possible range of seismic PSD amplitudes.

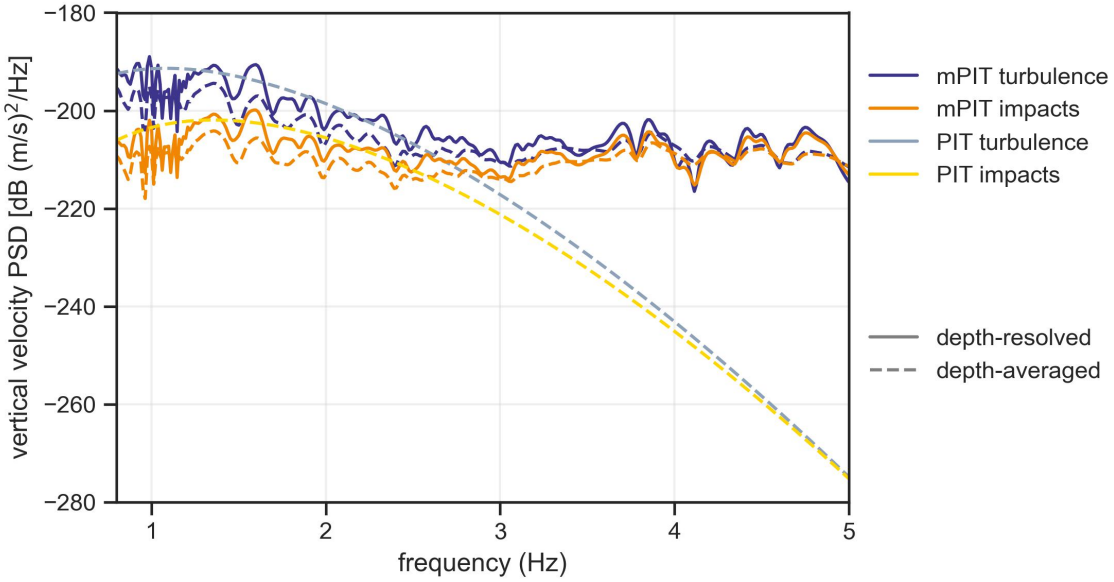

Figure 6 Comparison of mPIT PSDs for depth-resolved vs. depth-averaged steady-state solution. Depth-averaged steady-state inputs are also used for comparison between PIT and mPIT models, which are marked by the dashed lines in Figure 5. Differences between the PIT and mPIT models mainly come from the different Green's functions.

4.2 Effect of particle grain-size depth profile

Gestrich et al. (2020) found that one of the input fields that had the greatest impact on the tremor PSDs through the particle impacts force spectra was representative grain size. Not much is known about the distribution of grain size throughout the conduit, as well as how it varies over the course of the eruption. Lithics have been observed in erupted materials – likely due to erosion of the conduit walls during eruption – which would then introduce differently sized particles into the flow (e.g., Fee et al., 2017; Macedonio et al., 1994). Also, there has been some evidence of processes like secondary fragmentation, whereby fragmented particles collide with each other and the conduit walls, leading to further grain size reduction (Dufek et al., 2012; Bindeman, 2005). Therefore, we consider a few different grain size depth profiles in order to investigate the influence on the particle impacts PSD using the mPIT model.

The chosen grain-size profiles are shown in Figure 7. We use the same steady-state solution presented in the previous section. Therefore, the default-constant profile is the same and serves as our reference case. Gestrich et al. (2020) found that large grain sizes were needed to match observations, so the max-constant profile serves as the uppermost bound on reasonable grain size – and hence, the maximum possible PSD amplitude. The remaining two example profiles vary from the maximum grain size at fragmentation to the default grain size at the vent, capturing possible descriptions of secondary fragmentation. Since it is not well understood how grain size varies, we investigate how the functional form of this grain-size variation influences the resulting seismic PSD. We explore a linear decrease with decreasing depth (i.e., approaching vent):

$$D_r(z)|_{\text{linear}} = 1.4 \times 10^{-3} - \left(\frac{0.5 - 1.4 \times 10^{-3}}{d_f} \right) z, \tag{15}$$

and a exponential decrease:

$$D_r(z)|_{\text{exponential}} = \frac{0.5^{d_f/z}}{(1.4 \times 10^{-3})^{(1-d_f/z)}}. \tag{16}$$

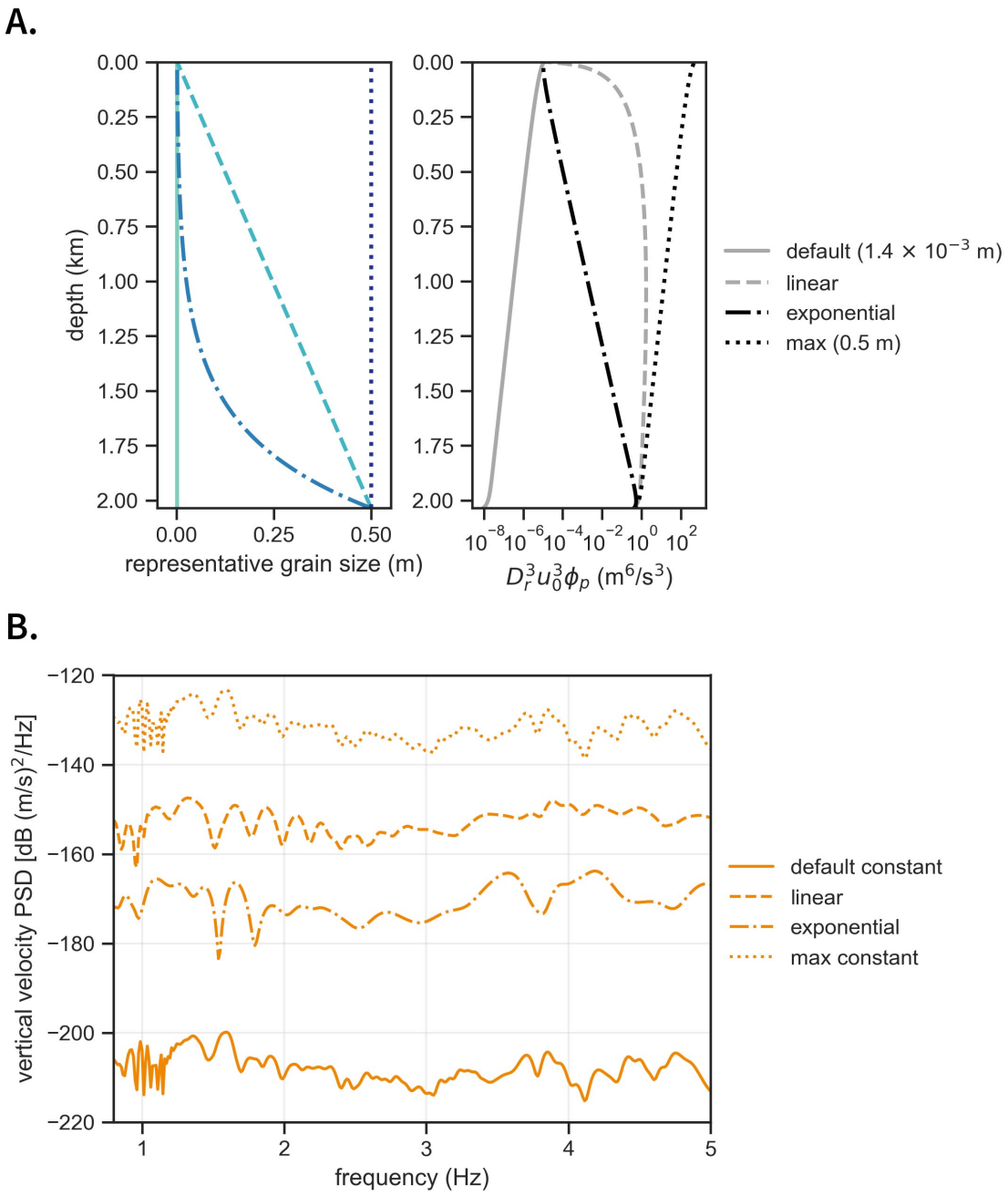

Figure 7 Effect of grain size variation with depth on impacts PSD using the steady-state solution shown in Figure 5. Note that the x-axis of the second panel in (a) is a log-scale. **A.** Grain size depth profiles. **B.** Impacts PSD for different profiles.

Consistent with Gestrich et al. (2020), we find that the representative grain-size profile has significant impact on the particle impacts seismic PSD (Figure 7). Comparing the two constant profiles, ~3 orders of magnitude difference in grain-size leads to 9 orders of magnitude difference in PSD amplitude. While the impact rate decreases for increasing grain size, more momentum will be imparted to the surrounding earth by the larger particles, all other flow properties being equal. The particle impacts' integrand depth profiles for the two constant profiles follow the same trend, with the largest contributions to the signal arising from the upper conduit where the flow velocity is greatest. However, how grain size varies with depth can potentially change where the largest contributions arise within the conduit. For the linear and exponential examples, the largest contributions come from just above fragmentation (Figure 7), indicating that the grain size depth profile has the most influence on the resulting integrand depth profile for these particular examples. The linear profile yields a higher PSD amplitude than the exponential one, as the grain size is larger at a given depth. Understanding the grain-size distribution proves to be critical in determining the predicted seismic PSD from this tremor source model.

During the high amplitude tremor phase of the 2016 Pavlof eruption (T1), the observed PSD amplitude ranges between approximately -110 dB and -140 dB. The max-constant profile comes closest to achieving these levels. While it exceeds the observed power in the higher frequencies (>2.5 Hz), it is not able to reach the peak power observed at lower frequencies. A uniform distribution of particles with radii on the order of 0.5 m throughout the upper conduit seems very unlikely to be present in real eruptions. Dufek et al. (2012) combine experimental results with numerical simulations to model volcanic particle break-up during an explosive eruption as a function of height above fragmentation depth. They found that the number of disruptive collisions (i.e., ones that would cause particle break-up) increased with increased initial particle diameter and increased fragmentation depth. For a particle with diameter of 0.1 m and fragmentation depth of 1 km, the expected number of collisions is on the order of 10^2 (Dufek et al., 2012). Given the maximum size of particles considered here (~1 m), one would expect an even higher number of disruptive collisions. This post-fragmentation break-up would lead to a decreasing grain-size profile as flow progresses up the conduit. As demonstrated here, decreasing grain-size profiles are likely to produce even smaller seismic PSD amplitudes.

4.3 Evolution of tremor during a waning eruption

While eruption tremor persists throughout an explosive eruption, its characteristics (e.g., amplitude) evolve as eruption dynamics change. Understanding this link is critical for developing more reliable methods for using eruption tremor monitoring to make real-time assessments of eruption explosivity. In this section, we explore how the evolving dynamics of a waning eruption are expressed in predicted tremor from the mPIT model. To approximately represent a waning eruption, we use solutions from our steady-state model with decreasing mass eruption rates to represent time snapshots of the input fields. This assumes that eruption waning is a quasi-steady process and does not capture dynamics associated with sudden eruption cessation from catastrophic collapse, for instance. Decreases in discharge rate are obtained by reducing chamber pressure. Since we are focused on the waning period, we choose all solutions to have subsonic flow out of the vent, with the highest mass eruption rate chosen to be somewhat close to the reference solution with choked flow. Vent pressure for all solutions is set to atmospheric pressure (10^5 Pa).

Figure 8 shows three "snapshots" of the waning eruption, where lower mass eruption rate indicates later time in

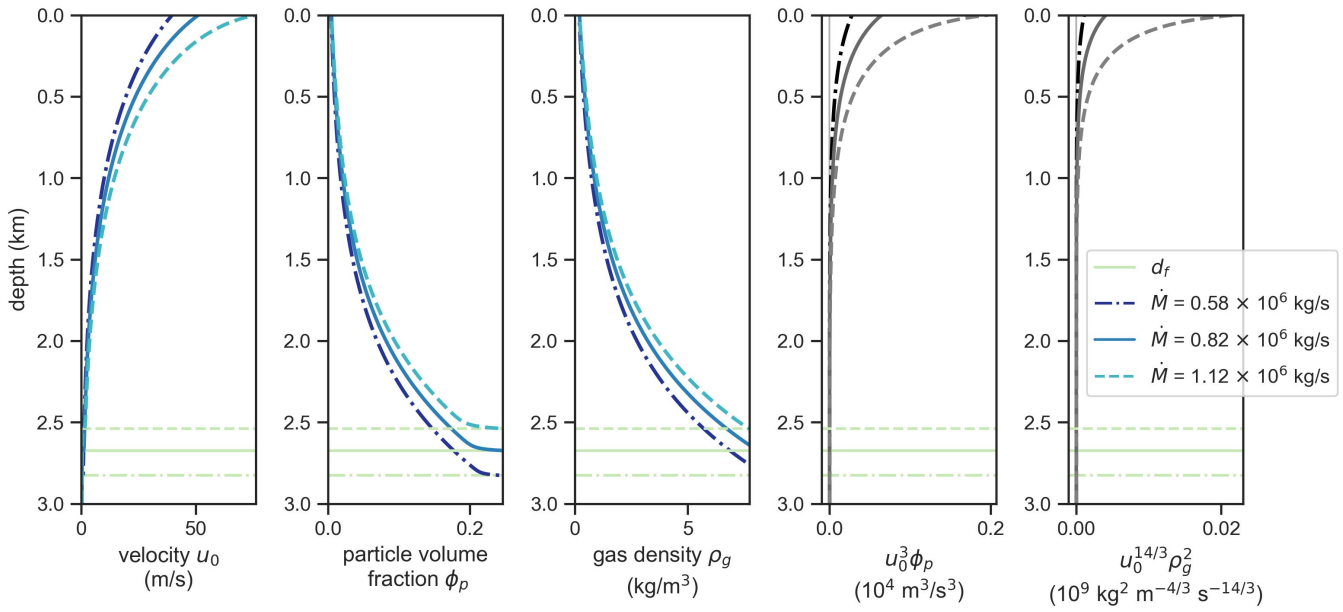

Figure 8 Input fields for steady-state solutions with different mass eruption rates $\dot{M}$, representing the waning of an eruption. Mach numbers at the vent are 0.45, 0.57, and 0.86 (with increasing mass eruption rate). Horizontal lines mark the fragmentation depth d_f.

the eruption. As magma is erupted, the chamber depressurizes and leads to the reduction of the driving pressure gradient. Flow slows as the driving pressure gradient decreases. For the particular fragmentation mechanism modeled here, depressurization throughout the conduit leads to descent of the fragmentation front through the conduit, and relief of the overlying weight leads to exsolution at greater depths (Figure 8). The final two panels in Figure 8 highlight that differences in particle impacts and turbulence force contributions come from the upper 1 km of the conduit, once again demonstrating the strong influence of the velocity profile. The change in fragmentation depth of several hundred meters has little effect.

As the eruption wanes and the velocity decreases, the amplitude of the seismic PSD decreases (Figure 9). We assume that the choked flow solution presented in Section 4.1 represents the most explosive period of the eruption and serves as a reference case for considering the tremor evolution during the eruption's waning. Note that mass eruption rate for this reference case is 1.92×10^6 kg/s with a Mach number of 1 at the vent. A 70% drop in mass eruption rate corresponds to a ~10 dB decrease in seismic power. Gestrich et al. (2020) aimed to develop an eruption tremor model that would be consistent with the hysteresis between tremor amplitude and plume height that was observed during the 2016 Pavlof eruption. To demonstrate that the PIT model was consistent with the observation of reducing tremor amplitude while plume height remained high – which the authors propose likely means that mass eruption rate remains high – they also considered the connection between eruption tremor and mass eruption rate. Their approach was to assume some constant mass eruption rate, select different combinations of values for input fields that would produce this mass eruption rate, and then look at the range of associated PSD amplitudes. They found a large range of amplitudes of tremor PSD that were consistent with a constant mass eruption rate. A downside of this approach is that input fields are tuned independently of one another without consideration for the common physical processes that cause covariation of the fields. However in this work, we take those processes into account through the conduit flow model and find that mass eruption rate is in fact correlated with the predicted tremor amplitude. High

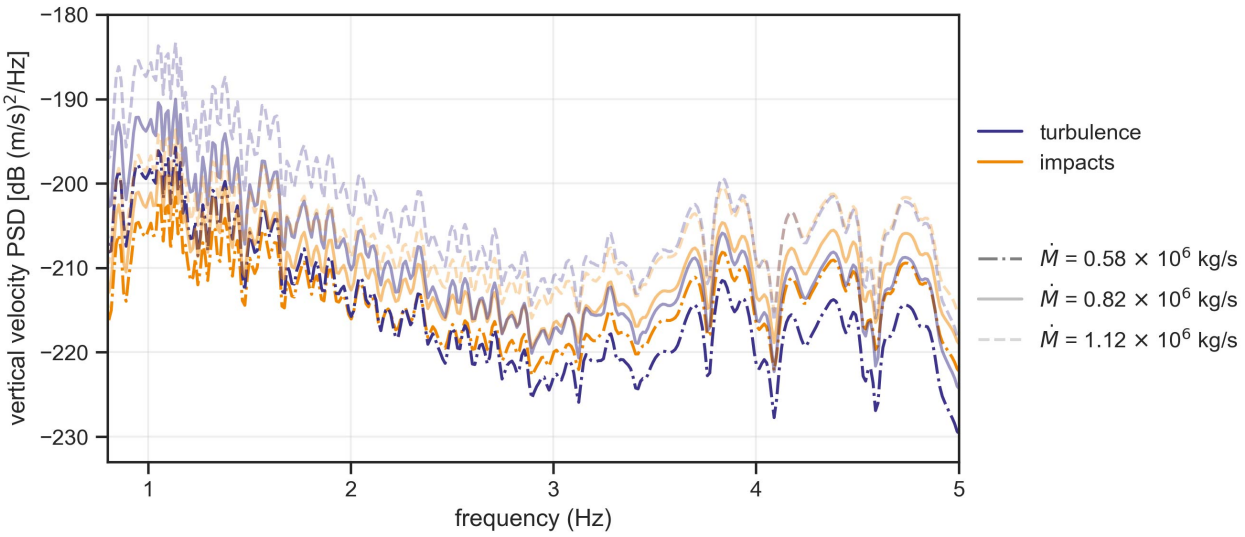

Figure 9 mPIT PSDs for steady state solutions with different mass eruption rates $\dot{M}$ shown in Figure 8. Note the smaller range of the y-axis compared with previous PSD plots.

mass eruption rate requires high flow velocity in the upper conduit, which is hugely influential on the predicted force spectra for this tremor model. Therefore, in order for tremor amplitude and mass eruption rate to become uncoupled to produce the observed hysteresis, evolution of particle size is required for the same mass eruption rate.

As mass eruption rate decreases, the relative importance of particle impacts vs turbulence contributions changes. For the example solution representing the most explosive phase, turbulence dominates the predicted tremor for frequencies less than 4 Hz (Figure 6) – almost an order of magnitude difference between the two contributions at peak frequency – with comparable contributions to particle impacts for higher end of the frequency band. This is consistent with the early stage of the waning period (i.e., solution with $\dot{M} = 1.12 \times 10^6$ kg/s); however, the transition point where the dominant contribution switches from turbulence to particle impacts is now shifted to a lower frequency of about 3.5 Hz. As the eruption continues to wane, the difference in power from the two contributions decreases and the transition frequency continues to shift to lower frequencies: 2.5 Hz for $\dot{M} = 0.82 \times 10^6$ kg/s and 2 Hz for $\dot{M} = 0.58 \times 10^6$ kg/s. However, rather than transitioning to comparable tremor contributions from turbulence and particle impacts in the higher frequencies, particle impacts increasingly become dominant. We can extrapolate that eventually the particle impacts will become dominant across the full frequency band as the eruption continues to wane. If alternative grain size distributions are considered, it could be possible that this transition point would occur earlier (or later) in the eruption. Therefore, understanding the evolution of grain-size distribution over the course of the eruption is critical for interpreting tremor source mechanisms using this model.

5 Conclusion

In this work, we expanded the particle impacts and turbulence (PIT) source model of eruption tremor presented in Gestrich et al. (2020). We replaced surface-to-surface Rayleigh wave Green's functions with full numerical Green's functions for a generic volcanic velocity model. This had significant impact on the shape of the predicted seismic PSD, producing a flatter spectrum across the 1-5 Hz frequency band of interest and more closely matching the shape of the observed seismic PSDs at the 2016 Pavlof eruption. This is caused by the increasing importance of body waves,

relative to surface waves, above 2-3 Hz. We also expanded the model to account for depth variation of the input fields – which we refer to as mPIT model – and applied this modified model to solutions from a steady-state conduit flow model. Utilizing steady-state conduit flow solutions as tremor model input ensures that we are considering the physical processes that relate the different input fields to one another and how those change with different eruption conditions. We found that conditions at the vent are often not representative of input fields throughout the region above fragmentation. The velocity profile had the greatest influence on the PSD amplitudes, meaning that the largest contributions to tremor arise from the very top of the conduit (at least for the default parameters considered). Therefore, the ranges of representative input values are likely even more restricted than the ones considered in Gestrich et al. (2020), limiting the possible range of predicted tremor PSD amplitudes. We also investigated the effect of the grain size distribution throughout the upper conduit by considering various grain-size depth profiles. As was found in Gestrich et al. (2020), grain size had significant effect on the predicted PSD. We also found that the grain-size depth profile could even affect where within the conduit had the dominant influence on the force spectra, potentially altering interpretation of the source of the seismic PSD. We still found that extreme parameter values are required to match the observed amplitude of eruption tremor during the 2016 Pavlof eruption. When exploring how the predicted tremor evolved over the course of a waning eruption, we found that the overall tremor PSD amplitude decreased with decreasing mass eruption rate. Given the strong influence of the velocity profile, the decoupling of tremor amplitude and mass eruption rate required to produce the hysteresis that was observed at Pavlof would have to arise from changes in particle size, as Gestrich et al. (2020) concluded. More study is required to place constraints on particle size and particle size distribution over the course of an eruption, in order to better evaluate the validity of this tremor source model.

Acknowledgements

This work was funded by the National Science Foundation (DGE-1656518 to Katherine Coppess, EAR-1930979 and EAR-2231849 to Eric M. Dunham). Computer simulations were performed on Stanford's Sherlock cluster and we gratefully acknowledge the support of staff at the Stanford Research Computing and funding from the Doerr School of Sustainability for these resources.

Data and code availability

The steady-state conduit flow code and analysis code for this work are hosted at the following (respectively): https://github.com/fredriclam/compressible-conduit-steady and https://github.com/kcoppess/mPIT-tremor-model. Seismic data from 2016 Pavlof eruption were downloaded from https://ds.iris.edu/mda/AV/.

References

Bindeman, I. N. Fragmentation phenomena in populations of magmatic crystals. *American Mineralogist*, 90(11-12):1801–1815, 2005. doi: 10.2138/am.2005.1645.

Boore, D. M. and Joyner, W. B. Site amplifications for generic rock sites. *Bulletin of the seismological society of America*, 87(2):327–341, 1997. doi: 10.1785/BSSA0870020327.

Caplan-Auerbach, J., Bellesiles, A., and Fernandes, J. K. Estimates of eruption velocity and plume height from infrasonic recordings of the 2006 eruption of Augustine Volcano, Alaska. *Journal of Volcanology and Geothermal Research*, 189(1-2):12–18, 2010. doi: 10.1016/j.jvolgeores.2009.10.002.

Chouet, B. A. and Matoza, R. S. A multi-decadal view of seismic methods for detecting precursors of magma movement and eruption. *Journal of Volcanology and Geothermal Research*, 252:108–175, 2013. doi: 10.1016/j.jvolgeores.2012.11.013.

Coppess, K., Lam, F. Y. K., and Dunham, E. M. Seismic signatures of fluctuating fragmentation in volcanic eruptions. 2024.

Coppess, K. R., Dunham, E. M., and Almquist, M. Ultra and very long period seismic signatures of unsteady eruptions predicted from conduit flow models. *Journal of Geophysical Research: Solid Earth*, page e2022JB024313, 2022. doi: 10.1029/2022JB024313.

Costa, A. Viscosity of high crystal content melts: Dependence on solid fraction. *Geophysical Research Letters*, 32(22), 2005. doi: 10.1029/2005GL024303.

Dufek, J., Manga, M., and Patel, A. Granular disruption during explosive volcanic eruptions. *Nature Geoscience*, 5(8):561–564, 2012. doi: 10.1038/ngeo1524.

Fee, D., Haney, M. M., Matoza, R. S., Van Eaton, A. R., Cervelli, P., Schneider, D. J., and Iezzi, A. M. Volcanic tremor and plume height hysteresis from Pavlof Volcano, Alaska. *Science*, 355(6320):45–48, 2017. doi: 10.1126/science.aah6108.

Gestrich, J. E., Fee, D., Tsai, V. C., Haney, M. M., and Van Eaton, A. R. A physical model for volcanic eruption tremor. *Journal of Geophysical Research: Solid Earth*, 125(10):e2019JB018980, 2020. doi: 10.1029/2019JB018980.

Gimbert, F., Tsai, V. C., and Lamb, M. P. A physical model for seismic noise generation by turbulent flow in rivers. *Journal of Geophysical Research: Earth Surface*, 119(10):2209–2238, 2014. doi: 10.1002/2014JF003201.

Haney, M. M., Matoza, R. S., Fee, D., and Aldridge, D. F. Seismic equivalents of volcanic jet scaling laws and multipoles in acoustics. *Geophysical Journal International*, 213(1):623–636, 2018. doi: 10.1093/gji/ggx554.

Hess, K. and Dingwell, D. B. Viscosities of hydrous leucogranitic melts: A non-Arrhenian model. *American Mineralogist: Journal of Earth and Planetary Materials*, 81(9-10):1297–1300, 1996.

Ichihara, M. Seismic and infrasonic eruption tremors and their relation to magma discharge rate: A case study for sub-Plinian events in the 2011 eruption of Shinmoe-dake, Japan. *Journal of Geophysical Research: Solid Earth*, 121(10):7101–7118, 2016. doi: 10.1002/2016JB013246.

Lesage, P., Heap, M. J., and Kushnir, A. A generic model for the shallow velocity structure of volcanoes. *Journal of Volcanology and Geothermal Research*, 356:114–126, 2018. doi: 10.1016/j.jvolgeores.2018.03.003.

Macedonio, G., Dobran, F., and Neri, A. Erosion processes in volcanic conduits and application to the AD 79 eruption of Vesuvius. *Earth and planetary science letters*, 121(1-2):137–152, 1994. doi: 10.1016/0012-821X(94)90037-X.

Matoza, R. S. and Roman, D. C. One hundred years of advances in volcano seismology and acoustics. *Bulletin of Volcanology*, 84(9):86, 2022. doi: 10.1007/s00445-022-01586-0.

McNutt, S. R. Volcanic tremor amplitude correlated with eruption explosivity and its potential use in determining ash hazards to aviation. In *Volcanic Ash and Aviation Safety: Proceedings of the First International Symposium on Volcanic Ash and Aviation Safety*, pages 377–385, 1994.

McNutt, S. R. and Nishimura, T. Volcanic tremor during eruptions: Temporal characteristics, scaling and constraints on conduit size and processes. *Journal of Volcanology and Geothermal Research*, 178(1):10–18, 2008. doi: 10.1016/j.jvolgeores.2008.03.010.

Prejean, S. G. and Brodsky, E. E. Volcanic plume height measured by seismic waves based on a mechanical model. *Journal of Geophysical Research: Solid Earth*, 116(B1), 2011. doi: 10.1029/2010JB007620.

Tsai, V. C., Minchew, B., Lamb, M. P., and Ampuero, J.-P. A physical model for seismic noise generation from sediment transport in rivers. *Geophysical Research Letters*, 39(2), 2012. doi: 10.1029/2011GL050255.

Zhu, L. and Rivera, L. A. A note on the dynamic and static displacements from a point source in multilayered media. *Geophysical Journal International*, 148(3):619–627, 2002. doi: 10.1046/j.1365-246X.2002.01610.x.